Localization of the gate and selectivity filter of the full-length P2X7 receptor

Anja Pippel[a], Michaela Stolz[b], Ronja Woltersdorf[b], Achim Kless[c], Günther Schmalzing[b,1], and Fritz Markwardt[a,1,2]

[a]Julius Bernstein Institute for Physiology, Martin Luther University, D-06097 Halle/Saale, Germany; [b]Molecular Pharmacology, Rheinisch-Westfälische Technische Hochschule (RWTH) Aachen University, D-52074 Aachen, Germany; and [c]Grünenthal Innovation, Department of Drug Discovery Technologies, Grünenthal GmbH, D-52078 Aachen, Germany

Edited by Richard W. Aldrich, The University of Texas at Austin, Austin, TX, and approved January 25, 2017 (received for review June 27, 2016)

The P2X7 receptor (P2X7R) belongs to the P2X family of ATP-gated cation channels. P2X7Rs are expressed in epithelial cells, leukocytes, and microglia, and they play important roles in immunological and inflammatory processes. P2X7Rs are obligate homotrimers, with each subunit having two transmembrane helices, TM1 and TM2. Structural and functional data regarding the P2X2 and P2X4 receptors indicate that the central trihelical TM2 bundle forms the intrinsic transmembrane channel of P2X receptors. Here, we studied the accessibility of single cysteines substituted along the pre-TM2 and TM2 helix (residues 327–357) of the P2X7R using as readouts (*i*) the covalent maleimide fluorescence accessibility of the surface-bound P2X7R and (*ii*) covalent modulation of macroscopic and single-channel currents using extracellularly and intracellularly applied methanethiosulfonate (MTS) reagents. We found that the channel opening extends from the pre-TM2 region through the outer half of the trihelical TM2 channel. Covalently adducted MTS ethylammonium$^+$ (MTSEA$^+$) strongly increased the probability that the channel was open by delaying channel closing of seven of eight responsive human P2X7R (hP2X7R) mutants. Structural modeling, as supported by experimental probing, suggested that resulting intraluminal hydrogen bonding interactions stabilize the open-channel state. The additional decrease in single-channel conductance by MTSEA$^+$ in five of seven positions identified Y336, S339, L341C, Y343, and G345 as the narrowest part of the channel lumen. The gate and ion-selectivity filter of the P2X7R could be colocalized at and around residue S342. None of our results provided any evidence for dilation of the hP2X7R channel on sustained stimulation with ATP^{4-}.

P2X7 receptor | P2X7 receptor homology model | single-channel open probability | single-channel conductance | cysteine-scanning accessibility mutagenesis

Cytolytic pore formation by extracellular adenosine triphosphate (ATP) was first described in mast cells and was outright suggested to involve the activation and subsequent pore dilatation of a hypothetical ATP receptor channel (1). A similar ATP-triggered pore-forming activity was subsequently found in many immune and inflammatory cells and certain transformed cell lines. The distinctive feature that is unique to this tentatively termed P2Z receptor (2) is that brief application of ATP (in its tetraanionic form, ATP^{4-}) evokes depolarizing cation fluxes, whereas prolonged application of ATP^{4-} causes formation of cytolytic pores with a molecular cutoff of ∼900 Da (for review, see ref. 3). The cytolytic activity was eventually assigned to the P2X7 receptor (P2X7R), the seventh and final member of the P2X receptor family. In HEK293 cells, the recombinant P2X7R conferred the same responses that were attributed previously to the P2Z receptor, including the dual-mode operation as a cation channel and a cytolytic pore (4, 5). Today, it is widely believed that P2X7R can mediate apoptotic or necrotic cell death under pathophysiological conditions (4–6).

The cytolytic activity of human P2X7R (hP2X7R) has been attributed to a time-dependent dilation of the integral ion channel based on macroscopic current recordings of various cell types (7–11). Particularly revealing was the observation that substituting T348 and D352 with basic residues in the channel-lining second transmembrane domain (TM2) of the rat P2X7R (rP2X7R) simultaneously increased the permeability of the normally cationic channel for Cl^- and an acidic fluorescent dye with an effective diameter of >10 Å (12). A "channel-to-pore" dilatation that changed the permeation characteristic from small inorganic cations (e.g., Na^+, K^+, and Ca^{2+}) to large organic cations [e.g., *N*-methyl-D-glucamine ($NMDG^+$)] has also been found for P2X2, P2X2/X3, and P2X4 receptors (13, 14) and certain transient receptor potential (TRP) channels (15, 16). In contrast, in extended single-channel recordings, we were unable to detect a single-channel correlate of pore dilation (17, 18). An unexpected explanation for the discrepancy between macroscopic and microscopic currents came from the seminal demonstration that V_{rev} shifts may reflect not pore dilatation but rather profound changes in the concentration of intracellular ions associated with prolonged P2XR activation (19). This study raises fundamental doubts about the existence of pore dilatation as a general property of P2XRs (20) and the related ion channels.

In this study, using substituted cysteine accessibility mutagenesis (SCAM) (21), we assessed whether peculiar conformational changes accompany ATP^{4-}-gated opening of the transmembrane permeation pathway in hP2X7R. The transmembrane domain of all P2X subunits consists of two helices, TM1 and TM2, which are connected by a large extracellular loop comprising the sequence elements that shape the intersubunit binding pockets for the natural ligand ATP. The N and C termini are intracellularly located. The apo-closed and ATP-liganded open X-ray structures

Significance

The P2X7 receptor (P2X7R) was the first ion channel that was suggested to transform from cation selective into nonselective by undergoing a dilatation in the diameter of its transmembrane pathway following sustained activation. This change requires that the selectivity filter behave as a dynamic structure. Here, we used a single-channel analysis of cysteine substitution mutants to find that the gate and selectivity filter of P2X7R are colocalized and primarily determined by one single residue, S342. We found the agonist-opened selectivity filter to be completely stable over time, indicating that use-dependent dilatation of the channel diameter does not occur. Instead, P2X7R exhibits striking susceptibility to remain in the open state for longer when the channel pore contains slowly or nonpermeating cations.

Author contributions: A.K., G.S., and F.M. designed research; A.P., M.S., R.W., and F.M. performed research; A.K. calculated the 3D P2X7 models; A.P., G.S., and F.M. analyzed data; and G.S. and F.M. wrote the paper.

The authors declare no conflict of interest.

This article is a PNAS Direct Submission.

[1]G.S. and F.M. contributed equally to this work.

[2]To whom correspondence should be addressed. Email: Fritz.Markwardt@medizin.uni-halle.de.

This article contains supporting information online at www.pnas.org/lookup/suppl/doi:10.1073/pnas.1610414114/-/DCSupplemental.

of a truncated zebrafish P2X4 receptor (ΔzfP2X4R) (22, 23) combined with a homology structure-based interpretation of the functional data have verified that the ionic permeation pathway is defined by TM2 residues (12, 24–27). Three circularly assembled TM2 helices, each of which is donated by one of the three protomers of the trimeric P2X receptors, enclose the centrally located ion channel pore along the threefold symmetry axis (23). The TM1 helices are located peripherally to the TM2 ion channel pore. Accordingly, we confined our SCAM analysis to the TM2 helix and flanking sequences of the full-length hP2X7R subunit. We combined membrane current recordings in the whole-cell mode and in various excised patch clamp configurations by probing with various cysteine-reactive methanethiosulfonate (MTS) reagents to assess the accessibility of cysteine residues that were substituted in the TM2-lined channel from both sides of the membrane. We determined the single-channel properties of the MTS-responsive mutants to clarify the molecular mechanisms underlying the macroscopic channel modifications (17). In addition, we biochemically assessed the accessibility of substituted cysteine residues to a bulky cysteine-reactive fluorescent maleimide dye to identify cysteine residues that are accessible but not functionally responsive to MTS reagents. Our combined data define the ion channel pore and gating region of P2X7R and reveal ATP^{4-} triggered distinct widening of the pre-TM2 region and the trihelical TM2 channel that was completely stable over time. Partial results of this work were presented in a poster at the 58th Annual Meeting of the Biophysical Society in San Francisco (28).

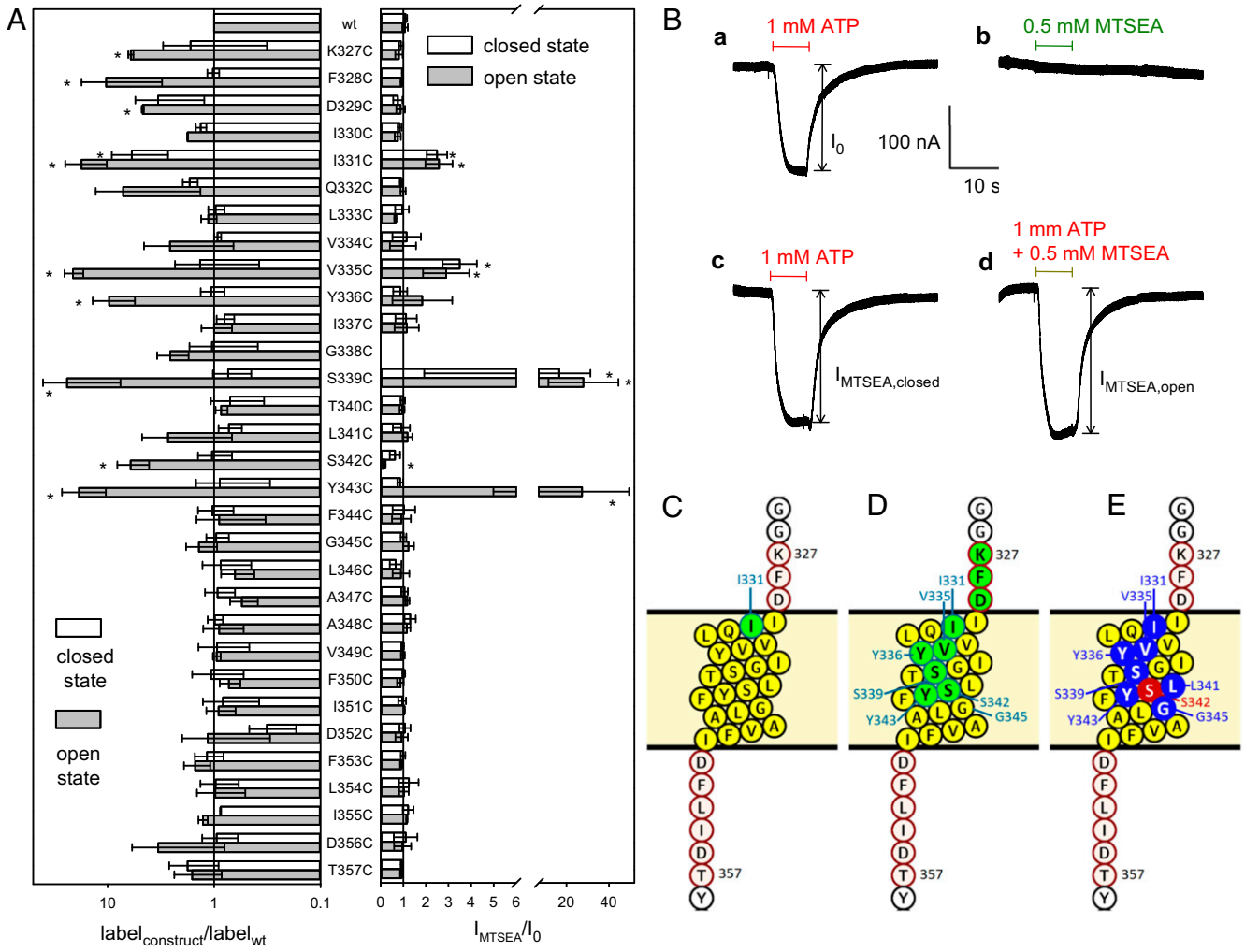

Fig. 1. Biochemical and TEVC screening for the accessibility of single-cysteine substitutions in the TM2 of the closed and ATP^{4-}-opened hP2X7R. (*A*, *Left*) Bars show the normalized means of the $Cy5^{-}$ fluorescence bound via maleimide chemistry to extracellularly accessible cysteine residues in the absence and presence of 1 mM ATP^{4-}, respectively, as normalized to the surface expression of the respective hP2X7R mutant (as assessed by lysine-bound Alexa Fluor 488 fluorescence). The specifically bound fluorescence levels were quantified through in-gel fluorescence scanning of the immunoprecipitated and SDS/PAGE-resolved mutants. (*Right*) State-dependent effect of $MTSEA^{+}$ (0.5 mM) on the 1 mM ATP^{4-}-elicited TEVC currents of the indicated SCAM mutant. Open and solid bars represent the means (n = 6–13 oocytes) of $I_{MTSEA,closed}$ and $I_{MTSEA,open}$, respectively, normalized to the I_0 of the corresponding hP2X7R construct. Means significantly different from 1 are marked by an asterisk. (*B*) The original $hP2X7R^{I331C}$ current traces illustrate the principle of the recordings: (*a*) response I_0 to ATP^{4-} without any $MTSEA^{+}$; (*b*), response of the closed hP2X7R to $MTSEA^{+}$; (*c*) response $I_{MTSEA,closed}$ to ATP^{4-} following $MTSEA^{+}$ preincubation; and (*d*) response $I_{MTSEA,open}$ to coapplied ATP^{4-} and $MTSEA^{+}$. (*C*–*E*) The TM2 helix of the hP2X7R (presented as extending from I330 to I351, filled yellow circles) and the red-framed flanking residues were individually mutated to cysteine. Residues of the apo-closed hP2X7R (*C*) and the ATP^{4-}-activated open hP2X7R (*D* and *E*) are colored according to their accessibility (in the cysteine-substituted form) to $Cy5^{-}$ maleimide in the biochemical experiments (green) or functional modulation by $MTSEA^{+}$ in electrophysiological experiments (blue and red, indicating current inhibition and stimulation, respectively). The ATP^{4-}-triggered accessibility of single cysteines engineered in pre-TM2 positions (^{327}K, ^{328}F, and ^{329}D) could be identified only biochemically. The TM2 segments were drawn using Protter at wlab.ethz.ch/protter/# (46).

Results

ATP^{4-} Increases Access to Cysteines That Were Engineered in Pre-TM2 and TM2 to $Cy5^{-}$ Maleimide. The X-ray structure of zfP2X4R indicates that the TM2 helix of the zfP2X4 subunit extends from residues Ile335 to Cys356 (23), corresponding to Ile330 to Ile351 of the hP2X7R subunit (23). A location shifted by only a few residues of the TM2 helix of the hP2X7R, V334–L354, is predicted by the topology algorithms included in the TOPCONS server (29). By including the flanking pre-TM2 and post-TM2 residues, we substituted a single cysteine at every residue from K327 to T357 of hP2X7R (see the hP2X7 topology cartoon, Fig. 1*C*). All 31 cysteine substitution mutants were incorporated into the plasma membrane (*SI Appendix*, Fig. S1, *Left*), and all but one, $hP2X7R^{G338C}$, responded to ATP^{4-} with an inward current at the standard holding potential of −40 mV (*SI Appendix*, Fig. S1, *Right*). Because of its defective state, the $hP2X7R^{G338C}$ mutant was not included in further analyses.

Next, we biochemically tested whether the single introduced cysteine residue in any of the hP2X7R TM2 mutants was accessible from the extracellular surface of intact *Xenopus laevis* oocytes by labeling with the bulky, thiol-reactive fluorescent dye sulfocyanine 5 ($Cy5^{-}$) maleimide (803 Da). $Cy5^{-}$ is anionic in nature overall (with two SO_3^- groups versus one quaternary N^+), and thus it is membrane impermeant. Because of the significant $Cy5^{-}$ maleimide labeling of the $hP2X7R^{wt}$, we normalized the covalently bound $Cy5^{-}$ fluorescence to the plasma membrane expression of each mutant, which we assessed by quantifying the covalent binding of the primary amino group-reactive compound Alexa Fluor 488 carboxylic acid, 2,3,5,6-tetrafluorophenyl ester, 5-isomer (Alexa Fluor 488 TFP). Alexa Fluor 488 is also anionic in nature due to its two SO_3^- groups and one COO^- group. When the channel was closed by the absence of ATP^{4-}, only one mutant, $hP2X7R^{I331C}$, incorporated significantly more expression-normalized $Cy5^{-}$ fluorescence than the $hP2X7R^{wt}$ (Fig. 1*A*, *Left*, open bar). However, when $Cy5^{-}$ maleimide labeling was performed in the presence of 1 mM ATP^{4-} for 30 min, a significantly increased level of bound $Cy5^{-}$ was observed for a total of nine hP2X7R TM2 mutants (Fig. 1*A*, *Left*, gray filled bars). In the rectangular and helical wheel projections, these extracellularly $Cy5^{-}$ maleimide-accessible residues extended through more than half of the TM2 (Fig. 1 *C* and *D*), and they all clustered on one face of the helix (*SI Appendix*, Fig. S2). Access to cysteine residues as deep as Y343C in the TM2 channel can be explained by the long and flexible aliphatic spacer arm of 10 or more methylene groups, by which the maleimide group is linked to the $Cy5^{-}$ fluorophore. This configuration allows the maleimide group to snorkel deep into the narrow channel to react with accessible cysteine residues, whereas the bulky, negatively charged $Cy5^{-}$ fluorophore is accommodated by the wider channel entrance. Notably, no cysteine that was introduced intracellularly to Y343C was significantly accessible for covalent labeling by $Cy5^{-}$ maleimide despite 30 min of costimulation with 1 mM ATP^{4-}. We infer from this observation that the selectivity filter is stable over time, indicating that marked dilatation of the channel's pore does not occur despite sustained stimulation with the high concentration of 1 mM ATP^{4-}.

MTS Ethylammonium$^+$ Delineates Similar ATP^{4-}-Dependent Cysteine Accessibility as Does $Cy5^{-}$ Maleimide. For a systematic screening of all of the mutants for their functional modification by the small positively charged MTS reagent, MTS ethylammonium$^+$ ($MTSEA^+$), we applied the two-electrode voltage-clamp (TEVC) method. $MTSEA^+$ covalently attaches an aminoethanesulfide moiety ($-S-CH_2-CH_2-NH_3^+$, 77 Da) to the cysteine sulfhydryl, thereby

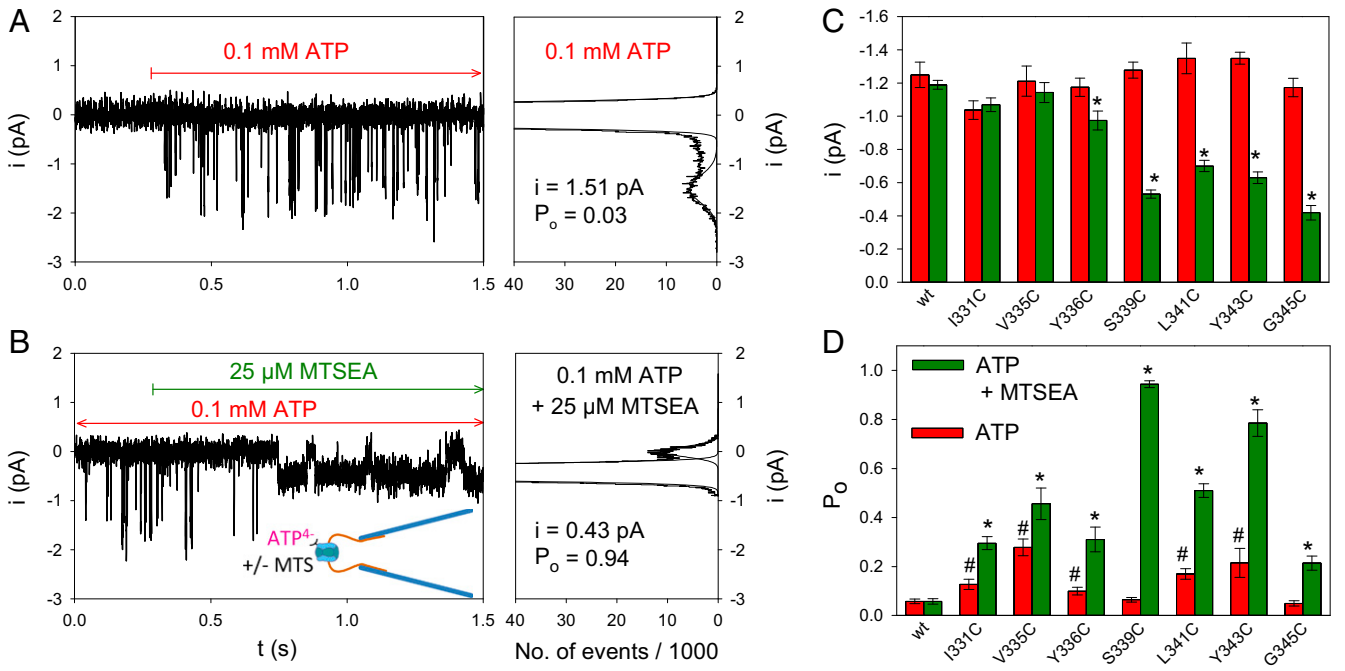

Fig. 2. Single-channel analysis of $MTSEA^+$ modifications in hP2X7R SCAM mutants. (*A and B*) Representative single-channel recordings (*Left*) and corresponding amplitude histograms (*Right*) from outside-out patches excised from an oocyte expressing $hP2X7R^{S339C}$. Single-channel currents were recorded following activation by 0.1 mM ATP^{4-} alone (*A*) or by coapplication of 0.1 mM ATP^{4-} and 0.025 mM $MTSEA^+$ (*B*). The indicated single-channel current amplitudes and the mean open probabilities were determined by fitting two Gaussian distributions to the data. (*Right*) Statistical comparisons of single-channel amplitudes (*C*) and open probabilities (*D*) determined during application of ATP^{4-} alone (red bars) or during coapplication of ATP^{4-} and $MTSEA^+$ (green bars). Each bar represents the means of 6–30 patches. The hashes indicate significant differences from $hP2X7R^{wt}$, resulting from the indicated cysteine substitution. The observed P_o changes may reflect small structural changes resulting from the cysteine substitutions and are not due to a decreased EC_{50} for ATP^{4-}, which was significantly diminished compared with the WT for only one mutant, $hP2X7R^{Y336C}$ (concentration–response curves in *SI Appendix*, Fig. S8). Asterisks indicate significant differences between the means with and without MTS.

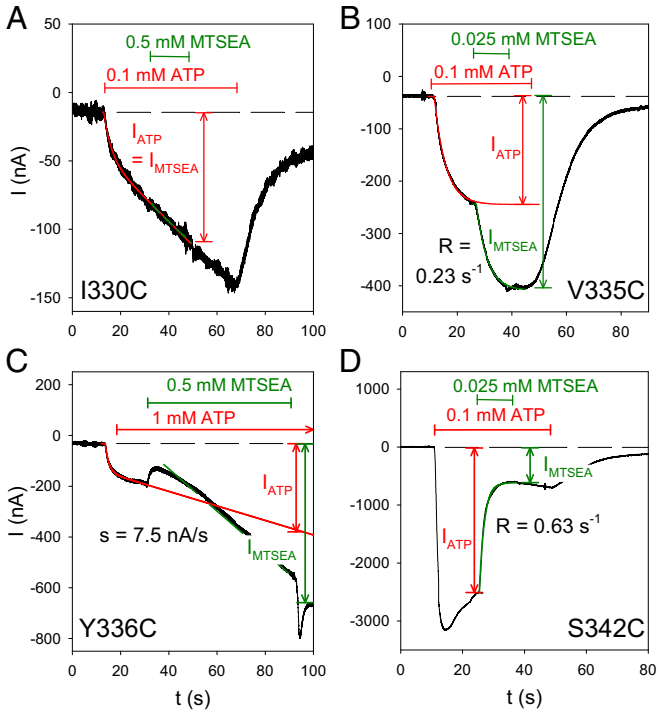

Fig. 3. Time course of $MTSEA^+$ modification for various hP2X7R SCAM mutants. Shown are representative TEVC current traces that were recorded from oocytes expressing the indicated hP2X7R mutant before, during, and after exposure to ATP^{4-} and $MTSEA^+$, as indicated. The specific mutants were selected to exemplify distinct current modifications by $MTSEA^+$ in the ATP^{4-}-induced open state as follows: (*A*) no current modification, (*B*) fast stimulation, (*C*) slow stimulation, and (*D*) inhibition. The time courses of the indicated current components I_{ATP} and I_{MTSEA} were fitted by the sum of an exponentially saturating increase and a linear component (33), as indicated by the overlaid lines. In *A*–*C*, the current component I_{ATP} was extrapolated to the end of the $MTSEA^+$ application. The R in *B* and *C* represents the rate constant of the $MTSEA^+$ effect; *s* in *C* denotes the slope of the $MTSEA^+$-induced current. We attribute the current deflections at the start and the end of the $MTSEA^+$ application in *C* to unspecific blocking and unblocking, respectively, of the $hP2X7^{Y336C}$-mediated current by $MTSEA^+$.

producing a lysine-like side chain that is positively charged at physiological pH values (21). With a minimum diameter of 4.6 Å, $MTSEA^+$ should be sufficiently small to permeate through the ATP^{4-}-opened hP2X7R channel, which has a mean diameter of ∼8.5 Å at its narrowest point (18). Hence, in principle, $MTSEA^+$ may be capable of reacting with all of the channel-lining substituted cysteine residues throughout the entire hP2X7R channel.

The sequential current responses to ATP^{4-} and $MTSEA^+$, each of which was followed by a 3-min washout period, are shown in Fig. 1*B* for the mutant $hP2X7R^{I331C}$. First, ATP^{4-} was applied to elicit the control current response I_0 (Fig. 1*B*, trace a); second, $MTSEA^+$ was applied alone to the closed-state hP2X7R (trace b); third, ATP^{4-} was applied to test whether the prior $MTSEA^+$ exposure modified the closed-state hP2X7R in a manner that noticeably affected the ATP^{4-}-gated current $I_{MTSEA,closed}$ (trace c); and fourth, ATP^{4-} and $MTSEA^+$ were coapplied to determine the $I_{MTSEA,open}$, indicating whether $MTSEA^+$ directly modified the current in the ATP^{4-} bound open state (trace d).

The overall data from the functional screening are summarized as open and filled bars, reflecting the modifying effect of $MTSEA^+$ at the closed and open channels, respectively (Fig. 1*A*, *Right*). Singly applied $MTSEA^+$ induced a significant current (>5 nA) in only one mutant, $hP2X7R^{S339C}$. This effect fully disappeared following washout, indicating that this $MTSEA^+$ stimulation was noncovalent in nature (*SI Appendix*, Fig. S3). The three mutants I331, V335C, and S339C were covalently modified by $MTSEA^+$ in the closed state, as indicated by the increased current response to the ATP^{4-} test pulse. In the ATP^{4-}-opened state, a total of seven hP2X7R mutants were modified by $MTSEA^+$ (Fig. 1*A*, *Right*, filled bars; see also Fig. 1*E*); five mutants (I331C, V335C, S339C, Y343C, and Y336C), exhibited a strongly and two mutants (L341C and G345C) a weakly enhanced current, and one mutant exhibited a significantly reduced current (S342C).

A small reduction in the ATP^{4-}-induced currents was observed in both the absence and presence of $MTSEA^+$ with eight additional hP2X7R mutants (K327C, D329C, I330C, L333C, L346C, F353C, D356C, and T357C) when repeatedly activated with ATP^{4-}. These small current reductions resulted from a $MTSEA^+$-independent current rundown intrinsic to these mutants following repeated exposure to ATP^{4-} (*SI Appendix*, Fig. S4). To exclude that the current rundown may have masked $MTSEA^+$ stimulation, we rescreened these mutants that were rated $MTSEA^+$ nonresponsive in our initial screening (Fig. 1*A*) by a time-resolved protocol (for details, see Fig. 3) (*SI Appendix*, Fig. S5).

Macroscopic Current Potentiation by $MTSEA^+$ Mirrors Increased Open-Channel Probability. The $MTSEA^+$ modifications of the ATP^{4-}-gated macroscopic currents in the cysteine hP2X7R mutants (Fig. 1*A*, *Right*) might reflect changes in the channel conductance, the open-channel probability, or both. To clarify this issue, we recorded single-channel events in outside-out patches that allow for the fast application and removal of ATP^{4-}.

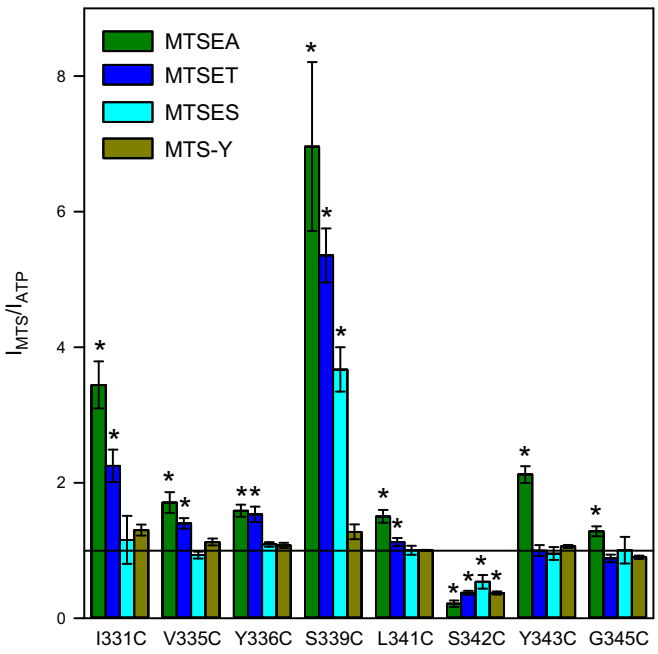

Fig. 4. Normalized effects of chemically diverse MTS reagents on ATP^{4-}-induced currents of hP2X7R SCAM mutants. The TEVC current components I_{ATP} and I_{MTS} were determined as illustrated in Fig. 3 *B*–*D*. Bars represent the means from 6 to 12 oocytes. A relative effect size of 1 (horizontal line) indicates that the current was not influenced by the MTS reagent. Asterisks indicate significant difference from 1. Because most of the MTS-modified cysteines are situated within the electrical field of the membrane (*SI Appendix*, Fig. S10), the cationic $MTSEA^+$ and $MTSET^+$ and the anionic $MTSES^-$ were applied at holding potentials of −40 mV and +20 mV, respectively, to provide an inwardly directed electrochemical driving force for all three charged reagents. The uncharged MTS-Y was applied at a holding potential of −40 mV. The concentrations of ATP^{4-} and MTS reagents used here are included in *SI Appendix*, Table S1.

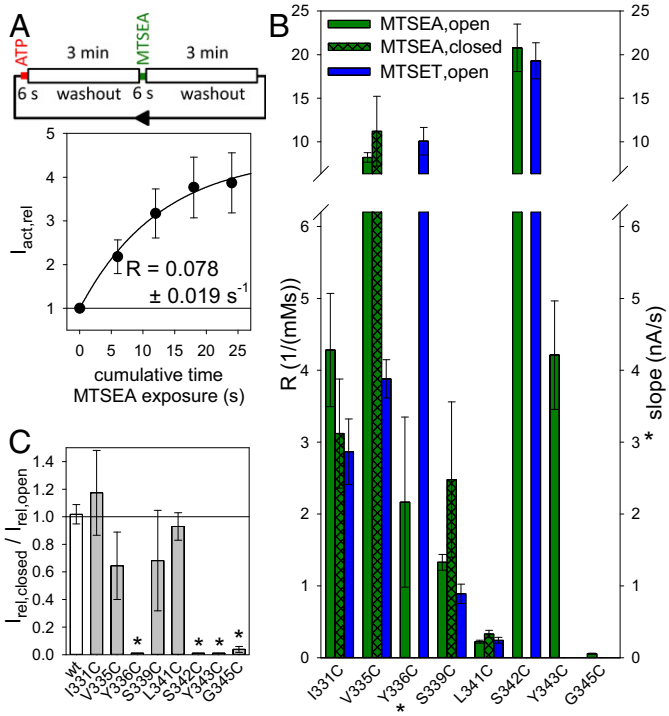

Fig. 5. MTS modification rates of hP2X7R SCAM mutants from the extracellular side. (*A*) The dependence of the ATP^{4-}-induced TEVC current on the cumulative time of exposure of the closed-state $hP2X7R^{I331C}$ to $MTSEA^{+}$. (*Top*) Schematic illustratration of one cycle of exposures for an $hP2X7R^{I331C}$-expressing oocyte to a 6-s lasting test pulse of 0.1 mM ATP^{4-}, followed by ATP^{4-} washout, a 6-s exposure to 0.25 mM $MTSEA^{+}$, and finally washout of the $MTSEA^{+}$ before the next test pulse of ATP^{4-} is applied. The time interval between the ATP^{4-} or $MTSEA^{+}$ applications was 3 min. The ATP^{4-}-elicited current amplitudes following each exposure to $MTSEA^{+}$ in the closed state ($I_{MTSEA,closed}$) were normalized to the current amplitude induced by the first test pulse of ATP^{4-} (at $t = 0$ s, i.e., before $MTSEA^{+}$ application, $I_{ATP,0}$) to yield $I_{act,rel} = I_{MTSEA,closed}/I_{ATP,0}$. The constant for the modification rate R of the closed channel by $MTSEA^{+}$ was obtained by fitting an exponentially saturating function (represented by the solid line) to the data. Data points are the means ± SEM of 8 oocytes from two different batches. (*B*) Statistical comparison of the modification rate constants for the indicated hP2X7R channel state by $MTSEA^{+}$ and $MTSET^{+}$. The rate constants R (*Left* ordinate) in the open and closed states were determined as illustrated in Fig. 3 *B* or *D* and in *A*, respectively. The modification rate at Y336C is represented by the slope s (*, *Right* ordinate), which was determined as shown in Fig. 3*C*. Bars represent the means ± SEM of 6–12 oocytes. (*C*) State dependence of $MTSEA^{+}$ modification. To assess the extent of the $MTSEA^{+}$ modification on the closed channel, the current amplitude induced by the fourth ATP^{4-} test pulse (i.e., following an 18-s cumulative $MTSEA^{+}$ exposure) was normalized to the amplitude of the first ATP^{4-} test pulse, as shown in *A*, to yield $I_{rel,closed} = I_{act,rel}(18\ s)/I_{act,rel}(0\ s) - 1$. $I_{rel,closed}$ was then normalized to the relative effect of $MTSEA^{+}$ on the current amplitude of the corresponding open state, $I_{rel,open}$, which is equal to $I_{MTSEA}/I_{ATP} - 1$ (taken from Fig. 4, green bars), i.e., $I_{rel,closed}/I_{rel,open} = (I_{act,rel}(18\ s)/I_{act,rel}(0\ s) - 1)/(I_{MTSEA}/I_{ATP} - 1)$. The values for the mutants Y336C, S342C, and Y343C were set to 0 because the ATP^{4-}-induced currents decreased slightly with repeated ATP^{4-} applications. This decrease was not significantly influenced by the continued presence of $MTSEA^{+}$ between the ATP^{4-} applications, thus indicating no effect of $MTSEA^{+}$ in the closed-channel configuration. Means are shown of 6–14 oocytes. Asterisks denote means significantly different from 1.

The hP2X7R-mediated single-channel currents in the outside-out patch can be identified by their fast and reproducible ATP^{4-}-dependent activation and deactivation (17, 18). Typical current traces are shown for the mutant $hP2X7R^{S339C}$ (Fig. 2 *A* and *B*). $MTSEA^{+}$ exerted two significant effects according to the histogram plots as follows: $MTSEA^{+}$ reduced the single-channel current amplitude and dramatically increased the open-channel probability simultaneously (Fig. 2 *A* and *B*). The increase in the open-channel probability apparently dominates over the decrease in the single-channel current amplitude and thus explains the net $MTSEA^{+}$-induced increase in the macroscopic ATP^{4-}-dependent current of $hP2X7R^{S339C}$. At the mutant $hP2X7R^{V335C}$, $MTSEA^{+}$ significantly increased the open-channel probability of $hP2X7R^{V335C}$ without significantly changing the single-channel current amplitude (*SI Appendix*, Fig. S6).

The bar graphs in Fig. 2 *C* and *D* summarize the average single-channel amplitudes (Fig. 2*C*) and open probabilities (Fig. 2D) of all of the mutants that responded to $MTSEA^{+}$ with a macroscopic gain of function. None of the single cysteine substitutions significantly affected the single-channel conductance (Fig. 2*C*). However, five of the seven substitutions, I331C, V335C, Y336C, L341C, and Y343C, led to a significantly higher open probability than $hP2X7R^{wt}$ (Fig. 2D). Following $MTSEA^{+}$ exposure, the single-channel current amplitude was unaffected when the substituted cysteine residues were located toward the extracellular entrance of the channel. However, starting with mutant $hP2X7R^{Y336C}$, $MTSEA^{+}$ caused a greater diminution of the single-channel amplitude (to less than 40% at G345C) when the substituted cysteine residues were located deeper in the channel toward its intracellular exit (Fig. 2*C*). This finding suggests a greater narrowing of the ion channel pore. The increase in the open probability was particularly pronounced for $hP2X7R^{S339C}$ and $hP2X7R^{Y343C}$, which achieved a P_o value close to 1 when exposed in the open state to $MTSEA^{+}$. Of note, the gating mechanism remained intact, as judged by the complete channel closure that occurred upon ATP^{4-} washout. The increase of the open probability is at least in part due to stabilization of the channel open state as inferred from the delayed deactivation time course (*SI Appendix*, *SI Results* and Fig. S7).

The sole mutant that responded to $MTSEA^{+}$ with a loss of function was $hP2X7R^{S342C}$, which could unfortunately not be subjected to histogram analysis because the ATP^{4-}-dependent single-channel events vanished within a few milliseconds following $MTSEA^{+}$ application (*SI Appendix*, Fig. S9). Therefore, it remains unknown whether the inhibiting effect of $MTSEA^{+}$ on $hP2X7R^{S342C}$ is due to a reduction in the single-channel current amplitude or a closing gating transition.

Open-State MTS Reactivity Locates the hP2X7R Selectivity Filter at or Just Internal to S342. To get detailed information about the kinetics of the $MTSEA^{+}$ effects, we determined the time course of the modification of the $MTSEA^{+}$-responsive mutants in the ATP^{4-} open state. We identified three distinct current modifications: (*i*) an increase to a higher current plateau (Fig. 3*B*), (*ii*) an acceleration of the linearly increasing current component (Fig. 3*C*), and (*iii*) a decline to a lower current plateau (Fig. 3*D*). The modifications persisted following $MTSEA^{+}$ washout, thus indicating their covalent nature. Notably, the channels' gates remained functional, as evidenced by the current decline upon ATP^{4-} washout (Fig. 3 *B* and *D*). The $MTSEA^{+}$-nonresponsive mutant $hP2X7R^{I330C}$ is shown as a negative control for comparison (Fig. 3*A*). To quantify the $MTSEA^{+}$ effect, we normalized the current amplitude I_{MTSEA} at the end of the $MTSEA^{+}$ exposure to the current amplitude I_{ATP} recorded in the absence of $MTSEA^{+}$ and extrapolated to the same time point, at which I_{MTSEA} was measured (Fig. 3 *A*–*D*).

To localize the selectivity filter and the gate of the hP2X7R, we applied the same kinetic protocol for determining the modification of the eight $MTSEA^{+}$-responsive hP2X7R mutants by three additional MTS reagents: $MTSET^{+}$, $MTSES^{-}$, and MTS-Y (4-hydroxybenzyl-MTS) (21). $MTSET^{+}$ and $MTSES^{-}$, which covalently add an ethyl-trimethylammonium group ($-S-CH_2-CH_2-N(CH_3)_3^{+}$, 119 Da) or an ethyl-sulfonate group ($-S-CH_2-CH_2-SO_3^{-}$, 140 Da) to cysteine sulfhydryls, have opposite charges, but they have identical space-filling diameters of 5.8 Å, i.e., larger than the 4.6 Å of

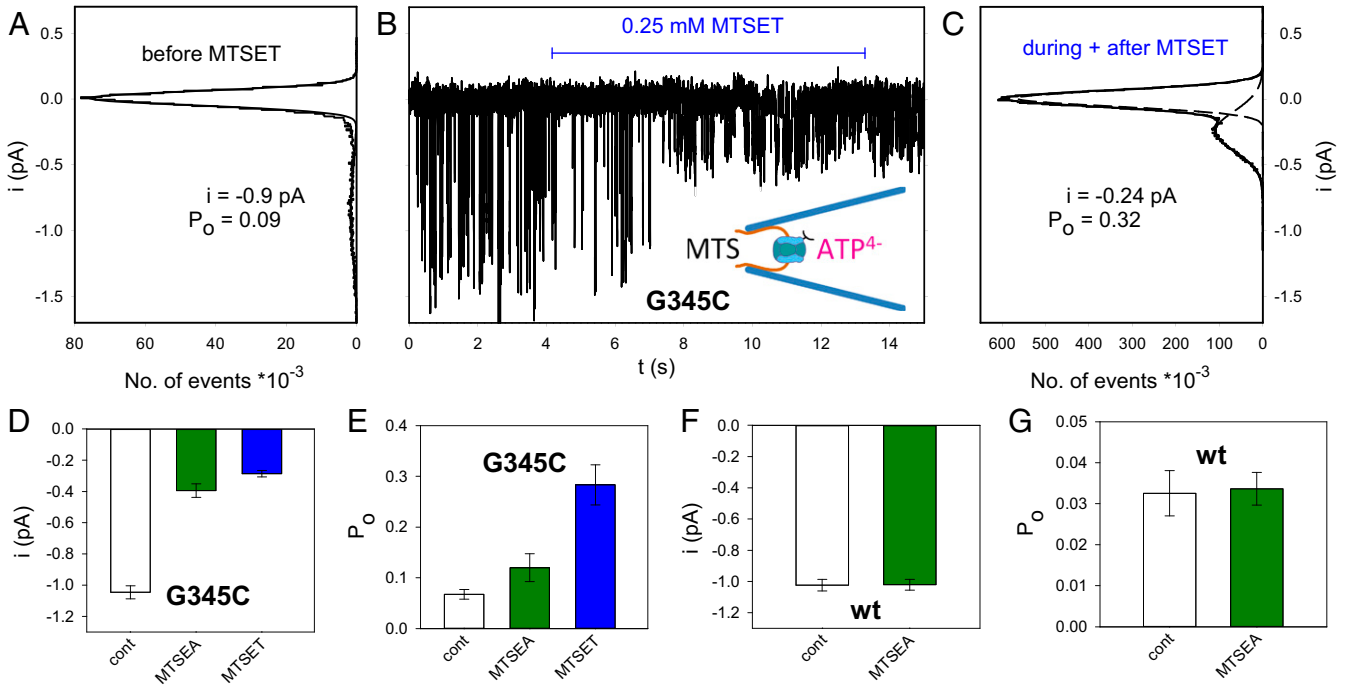

Fig. 6. hP2X7R^{G345C} single-channel modifications by MTS reagents bath applied to the intracellular side of inside-out patches. (*A*–*C*) The representative current trace in *B* was recorded from an inside-out patch excised with a patch pipette containing 0.1 mM ATP^{4-} to open the expressed hP2X7R^{G335C} channel. The onset and duration of the bath application of MTSET^{+} to the intracellular site of the inside-out patch is indicated by the horizontal bar. The single-channel current amplitudes and open probabilities were extracted from the amplitude histograms of the ATP^{4-}-induced single-channel events recorded before exposure to MTSET^{+} (*A*) and during and after exposure to MTSET^{+} (*C*). (*D*–*G*) The same experiments as indicated in *A*–*C* were also conducted with MTSET^{+} for the hP2X7R^{G345C} mutant and MTSEA^{+} for the hP2X7R^{wt}. Following MTSEA^{+} or MTSET^{+} exposure in the hP2X7R^{G345C} mutant, the derived single-channel amplitudes and the open-channel probabilities were significantly different from the nonexposed controls (*D* and *E*). In contrast, MTSEA$^{+/-}$ exposure did not modify hP2X7R^{wt} (*F* and *G*). Bars represent the means of 6–26 oocyte patches.

MTSEA^{+} (30). Compared with MTSEA^{+}, MTSET^{+} caused qualitatively similar but quantitatively smaller effects on six of the eight mutants (I331C, V335C, Y336C, S339C, L341C, and S342C) (Fig. 4 and Fig. 5*B*). At residues Y343C and G345C, which are positioned deeper in the channel with respect to the cell surface (Fig. 1), MTSET^{+} (in contrast to MTSEA^{+}) produced no significant effect (Fig. 4 and Fig. 5*B*).

The anionic MTSES^{-} functionally modified the two mutants S339C and S342C, which were stimulated and inhibited, respectively, i.e., in qualitatively the same manner as they were by the positively charged MTS reagents (Fig. 4). The uncharged but also bulky MTS-Y adds an ethyl-tyrosine group (S-CH_2-CH_2-C_6H_4-OH, 153 kDa), which converts a cysteine into a tyrosine-like residue. MTS-Y functionally affected only hP2X7R^{S342C}, which was blocked (Fig. 4).

The combined data indicate that the small MTSEA^{+} reagent can penetrate up to one helical turn deeper into the channel to access Y343C and G345C than the bulkier reagents. MTSET^{+}, MTSES^{-}, and MTS-Y reach S342C, but no cysteine that was introduced at a deeper position in the channel. That all three charged MTS reagents and the uncharged MTS reagent mediated an inhibition at S342C suggests that the steric hindrance is sufficient to block the channel at S342C. The finding that both oppositely charged MTS reagents can reach S342C charge independently indicates that the external border of the charge selectivity filter must be located at or just internally to Ser342. For a gain of function, the coupling of a charged moiety was crucial. Whereas a positive charge was stimulatory at the five gain-of-function positions I331C, V335C, Y336C, S339C, and L341C, the negative charge provided by MTSES^{-} was stimulatory only at S339C.

Accessibility of External MTS Locates the External Border of the Gate C Terminus at L341C. To localize the gate region of hP2X7R, we assessed the modification rate of extracellularly applied MTSEA^{+} at the closed hP2X7R mutants, as shown for hP2X7R^{I331C} (Fig. 5*A*). MTSEA^{+} covalently modified I331C, V335C, S339C, and L341C in the closed and open states at similar rates (Fig. 5*B*) and to similar extents (Fig. 5*C*) following a cumulative 18-s application of MTSEA^{+}. This state-independent accessibility of MTSEA^{+} to L341C but no deeper cysteine (Fig. 5*B*) locates the gate region C terminal to L341C. The inaccessibility of Y336C in the closed but not in the open state may be attributed to the iris-like gating motion of TM1 and TM2 (22), directing the sulfhydryl group of Y336C in an MTS-accessible position only in the open-channel state.

Compared with the state-independent accessibility of S339C for MTSEA^{+}, the bulkier MTSET^{+} modified the closed hP2X7R^{S339C} channel at a rate of only 0.036 ± 0.019 $mM^{-1}{\cdot}s^{-1}$, which is ~30 times slower than it is at the open channel. This finding indicates that the gating-dependent constriction of the ion pathway starts at S339C and is fully developed at S342C.

Internal MTS Locates the Internal Borders of the Gate and Selectivity Filters at S342–G345. Next, we assessed the extension of the filter and gate region toward the intracellular exit of the TM2 channel. To this end, we applied MTSET^{+} or MTSES^{-} via the patch pipette to the intracellular side of the channel in multichannel outside-out patches and then triggered the channel opening with extracellular ATP^{4-} (cartoon at the *Top* of *SI Appendix*, Fig. S11). From the multichannel recordings detailed in *SI Appendix*, *SI Results* and Fig. S11, we infer that both the intracellular border of the gate region and the selectivity filter are located C terminally to S342 and that the size selectivity filter is formed by S342.

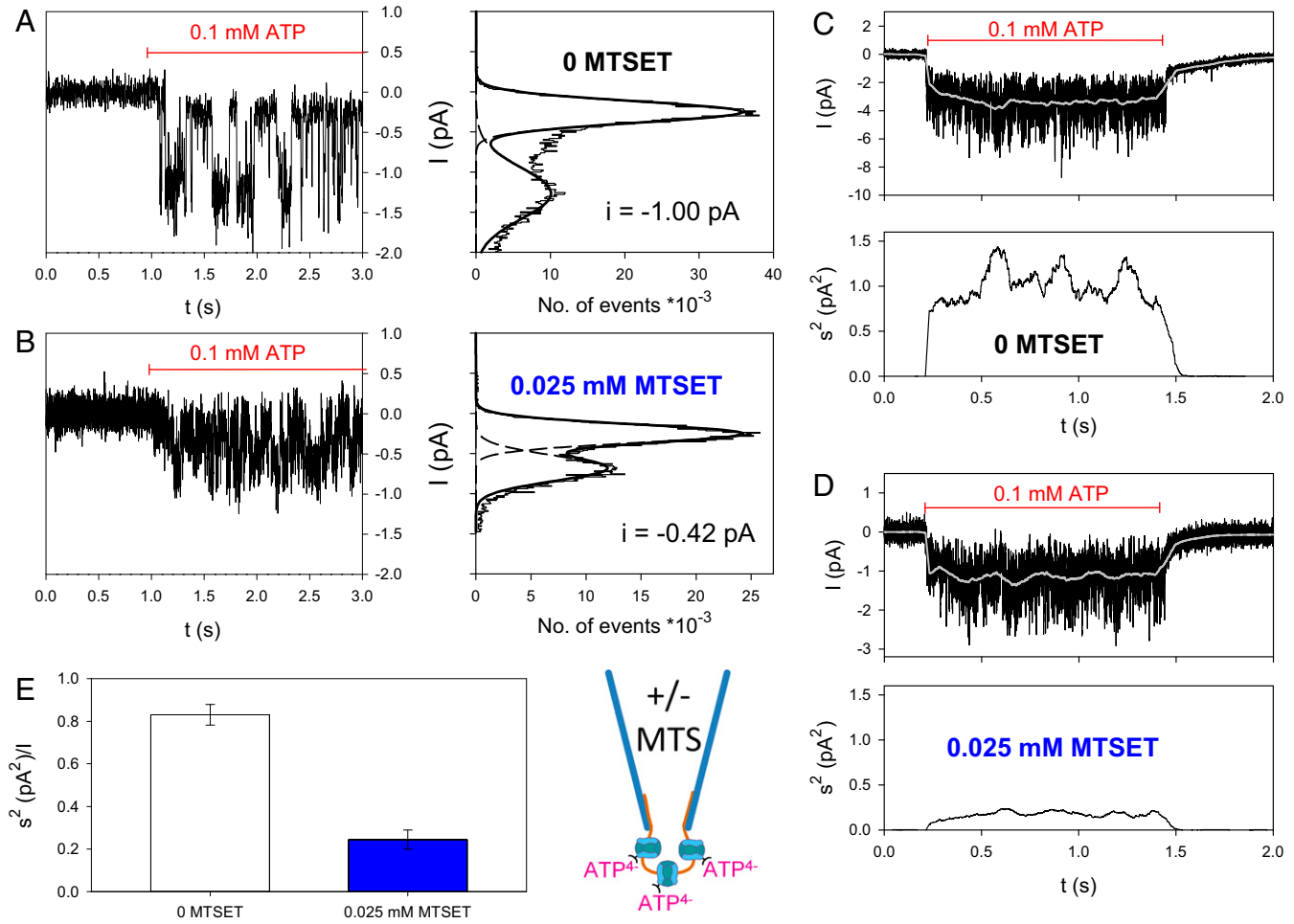

Fig. 7. hP2X7R^{G345C} single-channel modifications by MTS reagents that were pipette applied to the intracellular side of outside-out patches. (*A* and *B*) The representative current traces were recorded from inside-out patches excised from hP2X7R^{G335C}-expressing oocytes without MTSET$^+$ (*A*) and with 0.025 mM MTSET$^+$ (*B*) in the patch pipette. The horizontal bar indicates the period of ATP^{4-} application. The corresponding single-channel currents were calculated from the adjacent amplitude histograms. (*C–E*) Effect of intracellularly applied MTSET$^+$ on current noise kinetics. Shown are original traces recorded with pipette solutions without MTSET$^+$ (*C*) or with 0.025 mM MTSET$^+$ (*D*). The running average current I_{runavg} is shown as a white line. The corresponding time-dependent smoothed noise $\sigma^2{}_{runavg}$ is shown in the adjacent panels. (*E*) Statistics for the relative noise ($\sigma^2/I_{mean,500}$) of the first 500 ms during the very first ATP^{4-} application. The means from 16 and 7 patches excised without and with MTSET$^+$ in the pipette, respectively, are significantly different. For details, see *SI Appendix, SI Materials and Methods*.

Additionally, we tested the location of the internal borders of the gate and selectivity filter by making single-channel recordings. At hP2X7R^{G345C}, extracellular MTSEA$^+$ increased the ATP^{4-}-dependent currents only in the open state and only to a small extent (Figs. 4 and 5 *B* and *C*). Extracellular MTSET$^+$ modified neither the closed nor open channels at G345C (Figs. 4 and 5*B*), supposedly because of the poor permeation of MTSET$^+$ across the selectivity filter located N terminally from the G345 of the channel. To test whether MTS reagents can access G345C from the intracellular side, we activated hP2X7R^{G345C} currents in inside-out patches by including 0.1 mM ATP^{4-} in the recording patch pipette (schematic drawing in the *Center* of Fig. 6*B*). With application of MTSET$^+$ or MTSEA$^+$ to the bath and thus to the intracellular channel exit, the single-channel amplitude decreased and the open probability increased (Fig. 6 *A–E*). The modifying effect of 0.25 mM MTSET$^+$ developed within $t = 4.5 \pm 1.1$ s ($n = 9$ patches), corresponding to an approximate MTSET$^+$ rate constant of $R \sim 1/t/0.25$ mM $= 0.89$ mM^{-1}·s^{-1}. This result indicates that MTSET$^+$ modifies G345C from the intracellular side ~16-fold faster than the smaller MTSEA$^+$ from the extracellular side, where an effect rate constant of 0.055 mM^{-1}·s^{-1} was measured (Fig. 5*B*). A qualitatively similar effect was observed with intracellular MTSEA$^+$ (Fig. 6 *D* and *E*). These data support the view that the internal border of the selectivity filter is located N terminally to G345. At hP2X7R^{wt}, intracellular MTSEA$^+$ had no effect on the single-channel current amplitude or on the open probability (Fig. 6 *F* and *G*).

To define the channel gate toward the intracellular exit of the channel, we tested whether intracellular MTSET$^+$ (applied via the recording patch pipette) can modify G345C in the closed-state channel using outside-out patches. In the absence of intracellular MTSET$^+$, single-channel currents with the known mean current amplitude of the nonmodified hP2X7R^{G345C} were recorded (Fig. 7*A*). Approximately 2 min after the outside-out configuration was established with 0.025 mM MTSET$^+$ in the recording pipette, the very first ATP^{4-} application activated single-channel currents with a strongly reduced amplitude (Fig. 7 *B* vs. *A*). To quantify this effect, the ATP^{4-}-induced current noise was measured and found to be instantaneously lower when the pipette solution contained MTSET$^+$ (Fig. 7*D*) or was MTSET$^+$-free (Fig. 7*C*).

The mean relative noise during the first 500 ms of ATP^{4-} application, $\sigma^2/I_{mean,500}$, is a measure of the mean single-channel current amplitude (31, 32). A comparison indicates that the

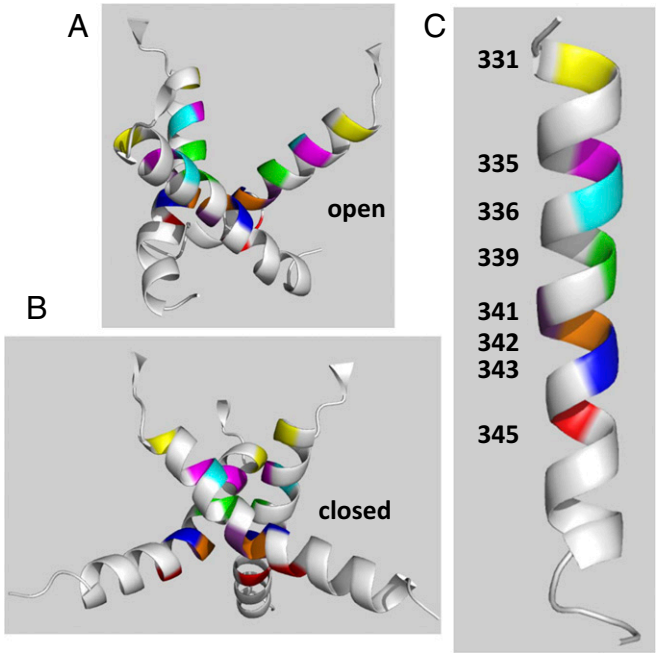

Fig. 8. Homology models of the pore-forming trihelical TM2 bundle of the hP2X7R. The ribbon diagrams were generated using PyMOL 1.3 (www.pymol.org). All of the residues that were functionally modified by $MTSEA^+$ when mutated to cysteine are colored with the same individual color. (*A* and *B*) Ribbon diagrams of the open and closed states of the hP2X7R channel (side views, extracellular side at top), derived from our hP2X7R homology models based on the apo and ATP^{4-}-bound X-ray structures of the ΔzfP2X4-C (22). (*C*) Schematic indications of the localizations of the functionally modified residues of the hP2X7R channel along one TM2 helix (from residue I331 to I351), as determined by SCAM analyses. The kink in the middle of the helix is oriented toward the viewer and therefore not visible.

noise-derived mean single-channel current amplitude was significantly smaller when $MTSET^+$ was present in the pipette solution (Fig. 7*D*, *Lower*) than in its absence (Fig. 7*C*, *Lower*). The mean patch current just as the smoothed noise displayed a monoexponentially rising time course with time constants of ∼40 ms. Once the plateau was attained, the current and noise stayed constant for 1 s (Fig. 7 *C* and *D*) and longer (up to at least 5 s, *SI Appendix*, Fig. S12). Based on the approximate modification rate constant for intracellular $MTSET^+$ of 0.89 $mM^{-1}{\cdot}s^{-1}$ (see above), 0.025 mM $MTSET^+$ can be calculated to react with G345C with a time constant of ∼45 s. This relatively slow reaction rate contrasts with the reduced current and noise that is evident from the very beginning of the ATP^{4-} test pulse. The only plausible explanation for this discrepancy is that $MTSET^+$ already has access to G345C when the channel is still closed after establishing the outside-out configuration and before the first ATP^{4-} application. These data place the internal border of the channel gate to a position that is N-terminal to G345, similar to the border of the selectivity filter.

Discussion

The Enigmatic Pore Dilation Has No Correlate at the Single-Channel Level. SCAM analyses of the TM2 helix have been successfully combined with homology modeling to probe the pore structure of P2X2R and P2X4R using MTS reagents as well as Ag^+ and Cd^{2+} for cysteine modification (for review, see refs. 24, 27). Our study applies the SCAM approach to probe the trihelical TM2 channel of P2X7R for shared similarities and potential differences with other P2XR family members. Its truly nondesensitizing behavior (17, 33, 34) makes hP2X7R ideally suited for combining SCAM with long-term recordings of single- and multichannel events in excised patches. In comparison, the paradigmatic P2X2R, though nondesensitizing in the whole-cell mode, inactivates rapidly in the excised patch mode apparently because of a diffusional loss of a cofactor (34, 35).

The favorable single-channel characteristics of the hP2X7R allowed us to place experimental focus on so-called progressive pore dilatation as an extraordinary feature of hP2X7R. This pore dilatation is generally deduced from a characteristic shift in the reversal potential V_{rev} of macroscopic currents that is virtually always observed when P2X7R-expressing cells are persistently activated in solutions containing large organic cations, such as *N*-methyl-D-glucamine ($NMDG^+$, diameter ∼9 Å) (11). In contrast, in extended single-channel recordings (up to 30 min), we noticed an entirely inconspicuous stable selectivity of $hP2X7R^{wt}$ for various ions, including the large cation tetramethylammonium (17, 18). In addition, none of our extensive SCAM experiments provided any hint that the intrinsic TM2 channel of the hP2X7R cysteine mutants progressively dilates over time in response to ATP^{4-} activation. The single-channel conductance remained absolutely constant during sustained ATP^{4-} activation even with the $hP2X7^{S339C}$ mutant, which exhibited a very high open probability of >0.9 in the $MTSEA^+$-modified form. One might argue that single-channel currents do not directly reflect the channel diameter. However, pore dilation without an associated change in the single-channel conductance appears rather unlikely, and, if it occurs, it is without functional significance. Our data demonstrate an entirely stable selectivity filter over time, thereby reinforcing our previous conclusion that the apparent pore dilatation is an epiphenomenon of whole-cell recordings (17). This view is now strongly substantiated by theoretical and experimental evidence indicating that the V_{rev} shifts in macroscopic recordings may reflect not pore dilatation but rather profound changes in the concentration of intracellular ions associated with prolonged P2XR activation. Regarding the P2X7R, there is firm evidence from our previous single-channel recordings that $hP2X7R^{wt}$ exhibits this critical feature when opened by ATP^{4-} to instantaneously exhibit significant permeability to large organic cations, including $Tris^+$ (17) and $NMDG^+$ (18).

The Pre-TM2 Region Is Gated by ATP^{4-} to Open a Wide Entrance to the Narrow TM2 Channel. Cysteines that were introduced into the pre-TM2 region K327–F328–D329 (K332–F333–N334 in zfP2X4R) were accessible for labeling with $Cy5^-$ maleimide in the ATP^{4-}-open state, but not in the apo-closed state. None of these three $Cy5^-$ maleimide-accessible residues was functionally modified by $MTSEA^+$. However, at I331C, which is located one helical turn deeper in the channel, $MTSEA^+$ was capable of modifying ATP^{4-}-induced single-channel currents. We infer from these data that the ATP^{4-}-gated opening transitions involve the pre-TM2 region, which seems to expand by exposing K327–F328–D329 to the extracellular environment. This view is supported by comparing the closed- and open-state models of hP2X7R, which reveals that the K327–D329 sequence moves from a maleimide-inaccessible position into a more maleimide-accessible position that allows for covalent binding of $Cy5^-$ fluorescent dye. This finding was best observed for residue D329 (*SI Appendix*, Fig. S13). It is plausible that $MTSEA^+$ also becomes covalently bound to residues K327C–F328C–D329C but that the channel entrance is too wide to allow bound $MTSEA^+$ to impede ion flow sterically or to influence gating. A wide channel entrance that is further expanded in the ATP^{4-}-bound open state can be observed in the X-ray structures of the ΔzfP2X4R-C (22) and is also evident in our hP2X7R homology models (*SI Appendix*, Fig. S14).

Gate and Selectivity Filters Are Primarily Determined by S342. The residues addressed in this section are displayed in the context of the X-ray structure-based homology model of the hP2X7R

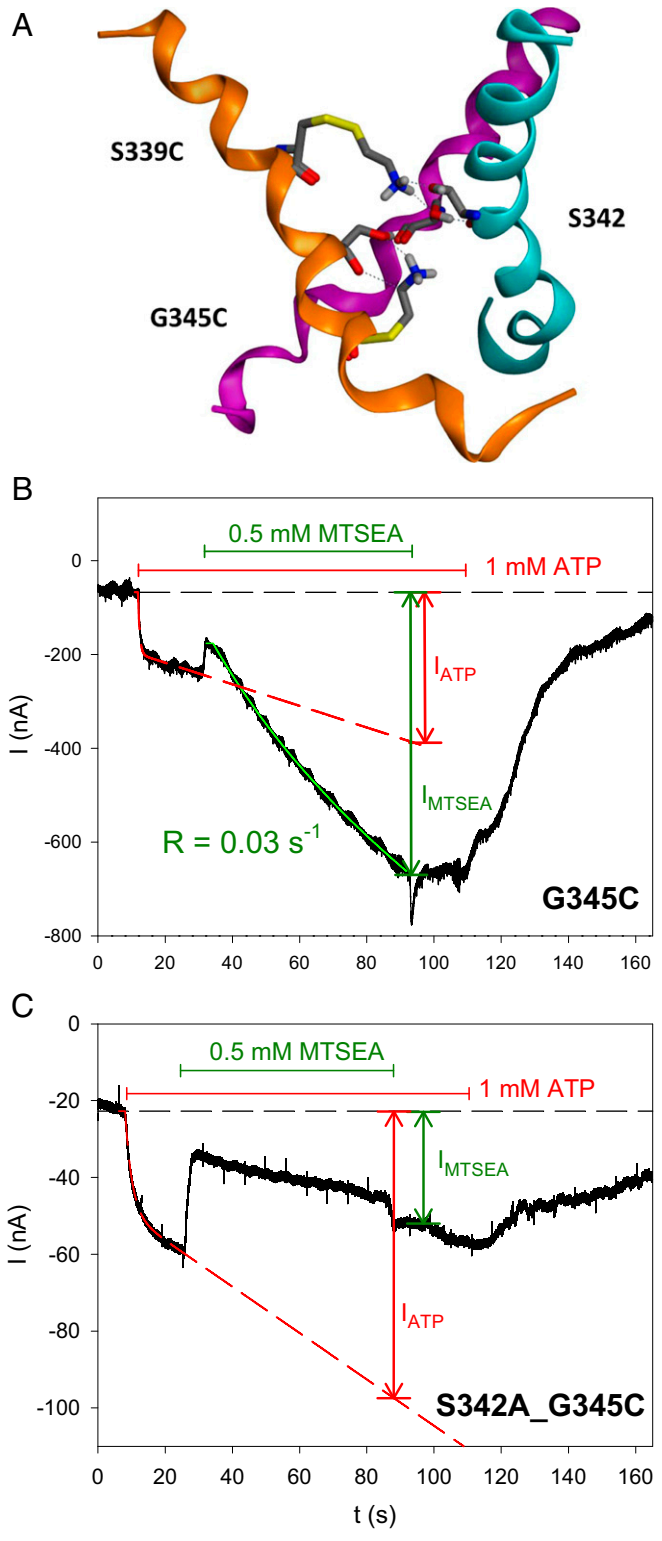

Fig. 9. Predicted hydrogen-bond interactions of cysteine-adducted $MTSEA^+$ with gating residue S342. (*A*) Ribbon diagram of the ATP^{4-} open state of the TM2 channel (side view, extracellular at *Top*) of our hP2X7R homology model, with each TM2 helix in a distinct color for easier identification. Stick representations (carbon in gray, amide and $MTSEA^+$ nitrogens in blue, carbonyl oxygens in red, sulfurs in yellow) of (*i*) the S342 of each helix and (*ii*) S339C and G345C with cysteine-adducted $MTSEA^+$ (of one helix only for clarity). The hydrogen atoms of the amino head group from $MTSEA^+$ form hydrogen bonds to side-chain hydroxyl oxygens and backbone carbonyl oxygens of S342. These $MTSEA^+$-mediated hydrogen bonds stabilize the open state of the hP2X7R channels, thus explaining the experimentally observed higher open-channel probability and the resulting potentiation of macroscopic currents. (*B* and *C*) Representative TEVC current traces. $MTSEA^+$ stimulated the linearly increasing current component of the ATP^{4-}-activated $hP2X7R^{G345C}$ mutant (*B*). Elimination of the hydroxyl group at S342, as realized in the $hP2X7R^{S342A,G345C}$ double mutant, reversed the $MTSEA^+$ effect from stimulation to inhibition (*C*).

channel for easier orientation (Fig. 8). The wide entrance appears to funnel into a narrower channel around I331C, which is the outermost cysteine residue that was functionally modified by $MTSEA^+$ in both the closed and open channels. At I331, the channel must be rather wide (*SI Appendix*, Fig. S15*A*) because the reaction of $MTSEA^+$ with I331C was noticeable only from the increase in the open-channel probability without indication of a steric inhibition of the cation flow. The closed channel is accessible from the extracellular side to $MTSEA^+$ and $MTSET^+$ as far down as L341C, but closed-state S339C reacts much slower with $MTSET^+$ than $MTSEA^+$; closed-state S342C is inaccessible to $MTSEA^+$. The functional data are fully consistent with the homology structure, indicating that (*i*) the closed channel narrows like a funnel from residue I331 via V335 to S339 (*SI Appendix*, Fig. S15 *A*–*C*) and (*ii*) the external boundary of the hP2X7R gate (the site where channel closing blocks ion flow) is located intracellularly to L341C. From the intracellular side of the closed channel, $MTSET^+$ accessed G345C, but not S342C. Accordingly, from both sides of the membrane, residue S342 is crucial in blocking permeation through the closed channel. A border of the gate, located two helical turns more extracellular, has been identified from the apo-closed ΔzfP2X4-B2 structure (23), with the gate region extending from L340 to A347 (V335 and S342 in hP2X7R, respectively) and A344 (S339 in hP2X7R), defining the constriction point of the channel. The constricted shape of this channel region with the location of the gate in the middle of the membrane fits well with our functional data. However, the ready accessibilities of V335C, S339C, and L341C to $MTSEA^+$ in the closed state locate the hP2X7R gate more toward the end of this region, at S342 (A347 in zfP2X4). For rP2X2R, virtually the same gate position at T336, T339, and S340 (S339, S342, and F343 in hP2X7R, respectively) has been proposed, according to the Ca^{2+} permeability (P_{Ca}/P_{Cs}) (36) and the access of thiol reagents, including Cd^{2+} (25, 26, 37).

The strong decrease in the single-channel current amplitude following $MTSEA^+$ modification of S339C, L341, Y343C, and G345C defines the region between S339 and G345, even in the ATP^{4-} open state, as a very narrow part of the channel. The open channel is reactive toward extracellular $MTSEA^+$ up to G345C, but toward bulkier MTS reagents only up to S342C. The access of extracellular and intracellular $MTSET^+$ to S342C and G345C, respectively, combined with the inaccessibility of extracellular $MTSET^+$ to Y343C and G345C assigns the selectivity filter of the open channel to S342 that when removed by mutation to cysteine, allowed $MTSET^+$ to access S342C. Accordingly, one single residue, S342, plays a crucial role as a gate and selectivity filter. A colocalization of the gate and selectivity filters was first deduced from P_{Ca}/P_{Cs} measurements at the rP2X2R (36) and later confirmed by other approaches (for references, see ref. 38). In particular, substitution of T339 in rP2X2R (S342 in hP2X7R) with a lysine converted the strong cation selectivity of the rP2X2 to weak anion selectivity; this finding suggests that the electrostatic environment around T339 is critical for the charge selectivity ions.

An overlay of the TM2 region of our hP2X7R homology model and the structure of the panda P2X7R (39) revealed only relatively small differences of the closed-state structures. In both structures, the ring formed by the three S342 residues represents the narrowest constriction of the closed channel (*SI Appendix*, Fig. S16). This similarity provides direct evidence that the zfP2X4R structure

is a reliable template for homology modeling of the hP2X7R channel and strengthens the validity of our conclusions.

The hP2X7R Channel Responds With Increases in Open Probability Rather Than Pore Dilatation. A surprising result of our work is that charged MTS reagents adducted to a cysteine residue that was introduced into the extracellular half of the TM2 channel can strongly increase the open probability. At all $MTSEA^+$-responsive mutants except S342C, the macroscopic current was potentiated relative to the control. Even at narrower parts of the channel (between S339C and G345C), the increase in the open probability overcompensated for the steric obstruction of the cation flow, thus explaining the observed macroscopic current increase.

A structure-based analysis of $MTSEA^+$ adducted to S339C or G345C revealed that the hydrogen atoms of the amino group of $MTSEA^+$ are in the sterically most favorable positions for hydrogen bonding interactions with both the hydroxyl group oxygen and the carbonyl oxygens of S342 (Fig. 9*A*). From this structural insight, we deduced that these hydrogen bonding interactions may be involved in locking the hP2X7R channel in an open configuration, as experimentally evidenced by the delayed closure of the $MTSEA^+$-adducted hP2X7R following ATP^{4-} washout (*SI Appendix*, Fig. S7). We could substantiate this prediction by demonstrating that the elimination of the hydroxyl group of S342 in the double mutant $hP2X7R^{S342A,G345C}$ reversed the $MTSEA^+$ effect from strong stimulation to strong inhibition (Fig. 9 *B* and *C*). Of note, $MTSEA^+$ reduced the macroscopic current of $hP2X7R^{S342A,G345C}$ ($34 \pm 5\%$) and the single-channel current amplitude of $hP2X7R^{G345C}$ ($36 \pm 5\%$, Fig. 2*C*), respectively, to virtually the same (not significantly different) extents. This finding suggests that the interaction of the adducted $MTSEA^+$ with S342 fully accounts for the increase in the probability of channel opening. We have previously observed a similar strong increase in the open probability of the hP2X7R in response to slowly permeating cations such as $Tris^+$ and $NMDG^+$, but it is unclear whether the mechanism is related. Taken together, these data indicate that hP2X7R exhibits surprising susceptibility to responding kinetically to slowly or nonpermeating intraluminal cations, but it lacks pore-dilating properties.

Materials and Methods

SI Appendix, SI Materials and Methods provides the reagents (40–42) and the methods, including the oocyte preparation (33); labeling and immunoprecipitation of hP2X7R (41, 43, 44); recordings of macroscopic and single-channel currents by TEVC (33) and patch clamping, respectively (17); patch noise analysis (31, 32); and homology-modeling (45) based on the two crystal structures of the ΔzfP2X4-C in the apo (closed) state [Protein Data Bank (PDB): 4DW0] (22) and the ATP-bound (open) state (PDB: 4DW1) (22).

ACKNOWLEDGMENTS. We thank the Deutsche Forschungsgemeinschaft (Ma1581/15-3; Schm536/9-3) for their financial support and GlaxoSmithKline for their kind permission to use the monoclonal antibody against the hP2X7R ectodomain.

1. Cockcroft S, Gomperts BD (1979) ATP induces nucleotide permeability in rat mast cells. *Nature* 279(5713):541–542.
2. Gordon JL (1986) Extracellular ATP: Effects, sources and fate. *Biochem J* 233(2):309–319.
3. Di Virgilio F (1995) The P2Z purinoceptor: An intriguing role in immunity, inflammation and cell death. *Immunol Today* 16(11):524–528.
4. Rassendren F, et al. (1997) The permeabilizing ATP receptor, $P2X_7$. Cloning and expression of a human cDNA. *J Biol Chem* 272(9):5482–5486.
5. Surprenant A, Rassendren F, Kawashima E, North RA, Buell G (1996) The cytolytic P_{2Z} receptor for extracellular ATP identified as a P_{2X} receptor ($P2X_7$). *Science* 272(5262): 735–738.
6. Adinolfi E, et al. (2005) $P2X_{(7)}$ receptor: Death or life? *Purinergic Signal* 1(3):219–227.
7. Alves LA, et al. (2014) The P2X7 receptor: Shifting from a low- to a high-conductance channel: An enigmatic phenomenon? *Biochim Biophys Acta* 1838(10):2578–2587.
8. Khadra A, et al. (2013) Dual gating mechanism and function of P2X7 receptor channels. *Biophys J* 104(12):2612–2621.
9. Sun C, Heid ME, Keyel PA, Salter RD (2013) The second transmembrane domain of P2X7 contributes to dilated pore formation. *PLoS One* 8(4):e61886.
10. Pelegrín P (2011) Many ways to dilate the P2X7 receptor pore. *Br J Pharmacol* 163(5): 908–911.
11. Virginio C, MacKenzie A, North RA, Surprenant A (1999) Kinetics of cell lysis, dye uptake and permeability changes in cells expressing the rat $P2X_7$ receptor. *J Physiol* 519(Pt 2):335–346.
12. Browne LE, Compan V, Bragg L, North RA (2013) P2X7 receptor channels allow direct permeation of nanometer-sized dyes. *J Neurosci* 33(8):3557–3566.
13. Khakh BS, Bao XR, Labarca C, Lester HA (1999) Neuronal P2X transmitter-gated cation channels change their ion selectivity in seconds. *Nat Neurosci* 2(4):322–330.
14. Virginio C, MacKenzie A, Rassendren FA, North RA, Surprenant A (1999) Pore dilation of neuronal P2X receptor channels. *Nat Neurosci* 2(4):315–321.
15. Chen J, et al. (2009) Pore dilation occurs in TRPA1 but not in TRPM8 channels. *Mol Pain* 5(3) doi: 10.1186/1744-8069-5-3.
16. Chung MK, Güler AD, Caterina MJ (2008) TRPV1 shows dynamic ionic selectivity during agonist stimulation. *Nat Neurosci* 11(5):555–564.
17. Riedel T, Lozinsky I, Schmalzing G, Markwardt F (2007) Kinetics of $P2X_7$ receptor-operated single channels currents. *Biophys J* 92(7):2377–2391.
18. Riedel T, Schmalzing G, Markwardt F (2007) Influence of extracellular monovalent cations on pore and gating properties of P2X7 receptor-operated single-channel currents. *Biophys J* 93(3):846–858.
19. Li M, Toombes GE, Silberberg SD, Swartz KJ (2015) Physical basis of apparent pore dilation of ATP-activated P2X receptor channels. *Nat Neurosci* 18(11):1577–1583.
20. Khakh BS, Lester HA (1999) Dynamic selectivity filters in ion channels. *Neuron* 23(4):653–658.
21. Karlin A, Akabas MH (1998) Substituted-cysteine accessibility method. *Methods Enzymol* 293:123–145.
22. Hattori M, Gouaux E (2012) Molecular mechanism of ATP binding and ion channel activation in P2X receptors. *Nature* 485(7397):207–212.
23. Kawate T, Michel JC, Birdsong WT, Gouaux E (2009) Crystal structure of the ATP-gated $P2X_{(4)}$ ion channel in the closed state. *Nature* 460(7255):592–598.
24. Browne LE, Jiang LH, North RA (2010) New structure enlivens interest in P2X receptors. *Trends Pharmacol Sci* 31(5):229–237.
25. Li M, Chang TH, Silberberg SD, Swartz KJ (2008) Gating the pore of P2X receptor channels. *Nat Neurosci* 11(8):883–887.
26. Li M, Kawate T, Silberberg SD, Swartz KJ (2010) Pore-opening mechanism in trimeric P2X receptor channels. *Nat Commun* 1(44):44.
27. Samways DS, Li Z, Egan TM (2014) Principles and properties of ion flow in P2X receptors. *Front Cell Neurosci* 8(6):6.
28. Markwardt F, Pippel A, Stolz M, Rahn T, Schmalzing G (2014) Function of the second transmembrane domain of the human P2X7 receptor. *Biophys J* 106(2):154a.
29. Bernsel A, Viklund H, Hennerdal A, Elofsson A (2009) TOPCONS: Consensus prediction of membrane protein topology. *Nucleic Acids Res* 37(Web Server issue):W465–W468.
30. Klein H, et al. (2007) Structural determinants of the closed KCa3.1 channel pore in relation to channel gating: results from a substituted cysteine accessibility analysis. *J Gen Physiol* 129(4):299–315.
31. Bretschneider F, Klapperstück M, Löhn M, Markwardt F (1995) Nonselective cationic currents elicited by extracellular ATP in human B-lymphocytes. *Pflugers Arch* 429(5):691–698.
32. Sigworth FJ (1980) The variance of sodium current fluctuations at the node of Ranvier. *J Physiol* 307(1):97–129.
33. Klapperstück M, Büttner C, Böhm T, Schmalzing G, Markwardt F (2000) Characteristics of $P2X_7$ receptors from human B lymphocytes expressed in *Xenopus* oocytes. *Biochim Biophys Acta* 1467(2):444–456.
34. North RA (2002) Molecular physiology of P2X receptors. *Physiol Rev* 82(4):1013–1067.
35. Ding S, Sachs F (2000) Inactivation of $P2X_2$ purinoceptors by divalent cations. *J Physiol* 522(Pt 2):199–214.
36. Migita K, Haines WR, Voigt MM, Egan TM (2001) Polar residues of the second transmembrane domain influence cation permeability of the ATP-gated $P2X_{(2)}$ receptor. *J Biol Chem* 276(33):30934–30941.
37. Kracun S, Chaptal V, Abramson J, Khakh BS (2010) Gated access to the pore of a P2X receptor: Structural implications for closed-open transitions. *J Biol Chem* 285(13): 10110–10121.
38. Jiang R, Taly A, Grutter T (2013) Moving through the gate in ATP-activated P2X receptors. *Trends Biochem Sci* 38(1):20–29.
39. Karasawa A, Kawate T (2016) Structural basis for subtype-specific inhibition of the P2X7 receptor. *elife* 5:e22153.
40. Buell G, et al. (1998) Blockade of human $P2X_7$ receptor function with a monoclonal antibody. *Blood* 92(10):3521–3528.
41. Stolz M, et al. (2015) Homodimeric anoctamin-1, but not homodimeric anoctamin-6, is activated by calcium increases mediated by the P2Y1 and P2X7 receptors. *Pflugers Arch* 467(10):2121–2140.
42. Grudzien-Nogalska E, et al. (2007) Synthesis of anti-reverse cap analogs (ARCAs) and their applications in mRNA translation and stability. *Methods Enzymol* 431:203–227.
43. Schmalzing G, Kröner S, Schachner M, Gloor S (1992) The adhesion molecule on glia (AMOG/beta 2) and alpha 1 subunits assemble to functional sodium pumps in Xenopus oocytes. *J Biol Chem* 267(28):20212–20216.
44. Fallah G, et al. (2011) TMEM16A(a)/anoctamin-1 shares a homodimeric architecture with CLC chloride channels. *Mol Cell Proteomics* 10(2):M110.004697.
45. Wolf C, et al. (2011) Molecular determinants of potent P2X2 antagonism identified by functional analysis, mutagenesis, and homology docking. *Mol Pharmacol* 79(4): 649–661.
46. Omasits U, Ahrens CH, Müller S, Wollscheid B (2014) Protter: Interactive protein feature visualization and integration with experimental proteomic data. *Bioinformatics* 30(6): 884–886.